

Probing Electroweak Phase Transition in the Singlet Standard Model via $b\bar{b}\gamma\gamma$ and $4l$ channels

Wenxing Zhang¹, Hao-Lin Li³, Kun Liu¹, Michael J. Ramsey-Musolf^{1,2}, Yonghao Zeng¹, Suntharan Arunasalam¹

¹*Tsung-Dao Lee Institute and School of Physics and Astronomy, Shanghai Jiao Tong University, 800 Dongchuan Road, Shanghai 200240, China*

²*Amherst Center for Fundamental Interactions, Department of Physics, University of Massachusetts, Amherst, MA 01003, USA*

Centre for Cosmology, Particle Physics and Phenomenology (CP3), Universite Catholique de Louvain

We investigate the prospects for resonant di-Higgs and heavy Higgs production searches at the 14 TeV HL-LHC in the combination of $b\bar{b}\gamma\gamma$ and $4l$ channels, as a probe of a possible first order electroweak phase transition in real singlet scalar extension of the Standard Model. Event selection follows those utilized in the $b\bar{b}\gamma\gamma$ and $4l$ searches by the ATLAS Collaboration, applied to simulation using benchmark parameters that realize a strong first order electroweak phase transition. The output of discriminant analysis is implemented by numerical calculation, optimised by the joint restriction from the two channels. The prospective reach for $b\bar{b}\gamma\gamma/4l$ channel could be more competitive in probing the electroweak phase transition at lower/higher resonance masses. With 3 ab^{-1} integrated luminosity, the combination of the $b\bar{b}\gamma\gamma$ and $4l$ channels can discover/exclude a significant portion of of the viable parameter space that realizes a strong first order phase transition when the resonance mass is heavier than 500 GeV.

I. INTRODUCTION

As the last piece of the Standard Model(SM), the Higgs boson was discovered in 2012 at the Large Hadron Collider(LHC) [1, 2]. The SM has achieved great success in describing a plethora of electroweak and strong interaction phenomena. However, the SM fails to explain a number of observable facts about the universe. Among these is the origin of the cosmic baryon asymmetry $Y_B = n_b/s$, whose present value is $Y_B = (8.59 \pm 0.11) \times 10^{-11}$ according to the PLANCK measurement [3]. This open puzzle provides one of the strong motivations to chase after a theory of physics beyond the SM.

One of the most well-studied and experimentally testable baryogenesis scenarios is electroweak baryogenesis (EWBG)[4–7], wherein Y_B is generated in conjunction with electroweak symmetry breaking (EWSB). For a review and references, see Ref. [8]. As with other baryogenesis scenarios, successful EWBG must satisfy the three "Sakharov criteria" [9, 10]: (1) baryon number violation; (2) C and CP-violation; and (3) departure from thermal equilibrium. The first two conditions guarantee that the net baryon number generation is possible. The last one is to ensure the net baryon number not be "washed out" by sphaleron process [11]. In EWBG, (3) is satisfied by the occurrence of a strong first order electroweak phase transition (SFOEWPT), which provides the conditions under which new CP-violating interactions generate the asymmetry. Within the SM, given the known mass of Higgs boson, the phase transition is a smooth crossover [10, 12]. To explain the magnitude of Y_B , new physics, especially those including new scalars coupling to the SM Higgs field, is essential to lead to a strong SFOEWPT. Based on general considerations, the presence of a first order EWPT implies that these particles must be lighter than $\sim 800 - 1000$ GeV and couple with sufficient strength to the Higgs boson, making them and their interactions a clear target for high energy collider studies[13].

The simplest realization of a SFOEWPT is achieved through adding one real singlet scalar in Higgs sector [14–17], which is called the real singlet-extended standard model (xSM). The scenario admits two pathways of EWSB: (i) a direct transition to the electroweak broken vacuum ("Higgs phase"), and (ii) a two-step first-order transition with the singlet scalar acquiring a vacuum expectation value (vev) before electroweak symmetry breaking. In either case, the singlet scalar may also obtain a vev in the Higgs phase. In the presence of a non-vanishing singlet vev, the singlet-like mass eigenstate and the SM-like mass eigenstate mix with each other after EWSB. Therefore, the LHC experiments searching for heavy scalar resonance shed light on exploring the viable parameter space for EWPT in the xSM [13]. Such experiments can be classified into several categories: (i) Di-Higgs channels with final states including $4b$ [18, 19], $bbVV^*$ [20–22], $bb\nu\bar{\nu}$ [21], WW^*WW^* [23], $bb\tau\tau$ [24, 25] and $bb\gamma\gamma$ [26, 27]. (ii) Di-boson channels with semileptonic final states [28, 29], hadronic final states [30, 31] and leptonic final states [22, 32, 33]. (iii) Di-fermion channels [34, 35]. On the other hand, studies have been performed for the parameter space that can realise the SFOEWPT. Heavy resonance mass up to 500 GeV can be observed by $bb\gamma\gamma$ and 4τ searches at the 14 TeV HL-LHC with luminosity equal to 3 ab^{-1} [16]. Also, in search for signals with $bbWW^*$ final state, the singlet-like scalar mass can reach 350 GeV at the 13 TeV, 3 ab^{-1} LHC [36]. For recent study in xSM, see in Ref. [16, 37–55].

Importantly, the singlet-like scalar will decay to conventional SM-like Higgs decay products due to singlet-doublet mixing as well as to di-Higgs final states (if sufficiently heavy). Thus, it is natural to ask how the combination of such "heavy Higgs" searches and resonant di-Higgs searches can further probe the SFOEWPT-viability in the xSM. In this

paper, we focus on the HL-LHC collider experimental tests on the xSM, including the $pp \rightarrow h_2 \rightarrow h_1 h_1 \rightarrow bb\gamma\gamma$ and $pp \rightarrow h_2 \rightarrow ZZ \rightarrow 4\ell$ final states. Our strategy in doing so is as follows. We restrict the doublet-singlet mixing angle θ by considering the current global Higgs searches and constraints from electroweak precision observables (EWPO)¹. We perform a global fit to the full parameter space by requiring the conditions for SFOEWPT and focus on the benchmarks that are constrained by both $bb\gamma\gamma$ and 4ℓ searches. We select benchmark points that produce maximum and minimum $bb\gamma\gamma$ cross section with resonance mass ranging from 260 GeV to 700 GeV, and perform simulation of the signal process by following [26, 28] to obtain the final distribution of signal event number. The background distribution are not obtained by simulation. Instead, we utilize the result in the experimental analyses reported in Ref. [26, 28].

As a preview, we summarise the main result in this paper:

- The discovery/exclusion upper limit for the heavy resonance mass reaches 300 GeV and 450 GeV for parameter space with minimum and maximum $bb\gamma\gamma$ cross section respectively.
- The discovery/exclusion upper limit for the heavy resonance mass reaches 750 GeV for the joint searches of the 4ℓ and $bb\gamma\gamma$ final states with minimum or maximum $bb\gamma\gamma$ cross section.

Our discussion of the analysis leading to these conclusions is organized as follows: In section II, we introduce the xSM framework and the various restrictions on the parameter space: perturbativity, global Higgs searches and EWPO. In section III, we consider the one-loop effective potential with high-T approximation and perform a general scan over the allowed parameter space to obtain regions compatible with a SFOEWPT. Section IV performs parameter scan with constraints from discribed above. Benchmark paramater choices yielding minimum and maximum $bb\gamma\gamma$ cross sections and SFOEWPT are listed in the end of this section. Section V performs the $bb\gamma\gamma$ and 4ℓ simulation based on 13 TeV experiments and extrapolates the result to 14 TeV 3000fb^{-1} . Section VI presents the discrimination between signal and background events. Further it draws conclusions about the sensitivity of exclusion ability. Section VII is dedicated to the conclusions. In the Appendix, subsection IX A and subsection IX B demonstrate the detail of the simulation of $bb\gamma\gamma$ and 4ℓ respectively. Subsection IX C calculates the impact from the current CDF-II W-boson mass measurement on the heavy Higgs mass and the mixing angle.

II. THE XSM MODEL

We consider a minimal extension of SM that includes a gauge singlet real scalar S . The most general renormalizable scalar potential is given by [15]

$$V_0(H, S) = -\mu^2(H^\dagger H) + \lambda(H^\dagger H)^2 + \frac{a_1}{2}(H^\dagger H)S + \frac{a_2}{2}(H^\dagger H)S^2 + \frac{b_2}{2}S^2 + \frac{b_3}{3}S^3 + \frac{b_4}{4}S^4, \quad (\text{II.1})$$

¹ A recent measurement of the W boson mass by the CDF-II collaboration deviates significantly the previous world average, which leads to difficulties in combining the measurement with previous results. Thus, in this work we will use the constraints from the fit of EWPO without including the newly measured W mass.

where H is the SM $SU(2)_L$ scalar doublet. The fields H and S obtain vevs after spontaneous EWSB. They may be cast into the form

$$S = \frac{1}{\sqrt{2}}(v_s + s), \quad (\text{II.2})$$

$$H = \begin{pmatrix} G^+ \\ \frac{1}{\sqrt{2}}(v_0 + h + iG^0) \end{pmatrix}. \quad (\text{II.3})$$

The a_1 and a_2 terms with a non-zero VEV of the singlet introduce mixing and a portal interaction between the SM Higgs and the singlet. The absence of a_1 and b_3 leads to a Z_2 symmetry that protects the singlet from mixing with SM particles if v_s vanishes, and hence the singlet becomes a DM candidate. However, even if the potential preserves the Z_2 symmetry explicitly, appropriate potential parameters can lead to a spontaneous Z_2 breaking, which yields a non-zero v_s and mixes the SM Higgs and singlet scalar through the a_2 term, thereby allowing the decay of both h_1 and h_2 to SM particles. For a recent analysis of this possibility, see Ref. [42]. A first order EWPT may arise in several ways [15, 56–59] (a) a one-step transition to the present Higgs phase wherein $v_s = 0$; (b) a one-step transition to a EWSB vacuum in which the vevs of both H^0 and S are non-vanishing; (c) a two-step transition, where the vacuum in the first step has $H^0 = 0$ and $S \neq 0$ while the vacuum at the end of the second step has $H^0 \neq 0$ and $S \neq 0$. Case (a) requires thermal loop contributions from S to generate a sufficiently large barrier between the symmetric and EWSB phases. For scenario (b), the cubic portal term can induce a tree-level barrier for $a_1 < 0$. The second step of the two-step history (c) will be first order due to the cross-quartic portal term with $a_2 > 0$. In the following, we study the SFOEWPT and its di-Higgs signal phenomenology.

The minimization (tadpole) conditions in xSM potential can be utilized to trade the two potential parameters μ^2 and b_2 with vevs of the two scalars:

$$\mu^2 = \lambda v_0^2 + (a_1 + a_2 x_0) \frac{x_0}{2}, \quad (\text{II.4})$$

$$b_2 = -b_3 x_0 - b_4 x_0^2 - \frac{a_1 v_0^2}{4x_0} - \frac{a_2 v_0^2}{2}. \quad (\text{II.5})$$

The mass matrix of the scalar sector can be derived by taking the second derivatives of the scalar potential and evaluating their value at the scalar vevs:

$$\mathcal{M}^2 = \begin{pmatrix} -\frac{a_1 v_0^2}{4x_0} + x_0(b_3 + 2b_4 x_0) & \frac{v_0}{2}(a_1 + 2a_2 x_0) \\ \frac{v_0}{2}(a_1 + 2a_2 x_0) & 2\lambda v_0^2 \end{pmatrix}. \quad (\text{II.6})$$

The above scalar mass matrix can be diagonalized by the mixing matrix parameterized by the mixing angle θ :

$$O(\theta)^T \mathcal{M}^2 O(\theta) = \begin{pmatrix} m_1 & 0 \\ 0 & m_2 \end{pmatrix}, \quad O(\theta) = \begin{pmatrix} \cos \theta & -\sin \theta \\ \sin \theta & \cos \theta \end{pmatrix}. \quad (\text{II.7})$$

where $m_1 = 125$ GeV corresponding to the mass of SM-like mass eigenstate. h_2 is the singlet-like mass eigenstate, such that the Higgs fields can be expressed as

$$h_1 = h \cos \theta + s \sin \theta \quad (\text{II.8})$$

$$h_2 = s \cos \theta - h \sin \theta, \quad (\text{II.9})$$

To guarantee the stability of the potential, the coefficient of the quartic field term should be positive definite, where the quartic field term is expressed as

$$V(h, s) \supset (h^2 \ s^2) \begin{pmatrix} \lambda & \frac{a_2}{4} \\ \frac{a_2}{4} & \frac{b_4}{4} \end{pmatrix} \begin{pmatrix} h^2 \\ s^2 \end{pmatrix}. \quad (\text{II.10})$$

The stability condition requires $a_2 \geq -2\sqrt{\lambda b_4}$.

III. ELECTROWEAK PHASE TRANSITION

The character of EWPT is understood in terms of the finite-T effective potential. It is well-known that in the conventional treatment, $V_{\text{eff}}^{T \neq 0}$, which is derived from the gauge-dependent 1PI effective action, suffers from gauge-dependence [38–41]. However, in the high temperature expansion, wherein the potential is expanded in powers of the temperature, the leading field- and temperature-dependent term that arises at $\mathcal{O}(T^2)$ is gauge-independent when evaluating the potential at the tree-level minimum of the fields according to the \hbar -expansion prescription [38]. For the same reason, the 1-loop zero-temperature Coleman-Weinberg potential, V_{CW} is also gauge independent. Therefore, in this paper, we employ the gauge-independent high-T approximated potential, which is composed of the tree-level potential, zero-temperature Coleman-Weinberg potential, V_{CW} , and the gauge-independent finite-temperature corrections expanded up to $\mathcal{O}(T^2)$.

We start by introducing the zero-temperature Coleman-Weinberg potential as follows:

$$V_{CW} = \sum_k \frac{(-1)^{2s_k}}{64\pi^2} g_k [M_k^2]^2 \left(\ln \frac{M_k^2}{\Lambda^2} + \frac{3}{2} \right), \quad (\text{III.1})$$

wherein the summation contains all fields that interact with the scalar fields h and s . The s_k is the spin of the particle, and M_k is the mass. The Λ is the renormalization scale, which is fixed to be v_0 .

The high-T approximation for bosonic fields and fermion fields are expressed according to [15]

$$V_{\text{High-T}}^{\text{scalar}} = \frac{g_s T^4}{2\pi^2} \left(-\frac{\pi^4}{45} + \frac{\pi^2 m_k^2}{12 T^2} - \frac{\pi}{6} \left(\frac{(m_k^2)^{3/2}}{T^3} \right) - \frac{m_k^4}{32T^4} \log \left(\frac{m_k^2}{c_B T^2} \right) \right) \quad (\text{III.2})$$

$$V_{\text{High-T}}^{\text{fermion}} = -\frac{g_f T^4}{2\pi^2} \left(-\frac{7\pi^4}{360} - \frac{\pi^2 m_k^2}{24 T^2} - \frac{m_k^4}{32T^4} \log \left(\frac{m_k^2}{c_F T^2} \right) \right) \quad (\text{III.3})$$

$$(\text{III.4})$$

respectively, where the $g_{s/f}$ is the number of degrees of freedom for scalars/fermions. We ignore the field-independent terms and keep the gauge-independent contributions up to the leading order of temperature. The high-T potential approximation then gives

$$V_{\text{High-T}} \simeq \frac{T^2}{24} (3M_g^2 + M_h^2 + M_s^2 + 6M_W^2 + 3M_Z^2) + \frac{T^2}{48} (12M_t^2), \quad (\text{III.5})$$

where the Goldstone, Higgs, and scalar masses are given by

$$M_g^2 = -\mu^2 + \lambda h^2 + \frac{s}{2} (a_1 + a_2 s) \quad (\text{III.6})$$

$$M_h^2 = M_g^2 + 2\lambda h^2 \quad (\text{III.7})$$

$$M_s^2 = b_2 + \frac{a_2}{2} h^2 + 2b_3 s + 3b_4 s^2, \quad (\text{III.8})$$

and where M_h^2 and M_s^2 are defined in eq.II.6. Note that after EWSB $M_g^2 = 0$, as can be seen from the tadpole conditions.

In the leading order of the high- T approximation, field-dependent thermal corrections appear in terms of quadratic in the scalar fields. By themselves, these thermal mass contributions do not generate a barrier between the origin and the global minima. Such a barrier can arise as follows, corresponding to the scenarios identified in Sec. II: (a) For the one-step direct transition to a pure Higgs phase, thermal loops, generated by the cross-quartic interaction proportional to a_2 , can enhance the SM contributions to the Th^3 -induced barrier; (b) for the one-step transition to the mixed vev-vacuum, the Z_2 breaking interactions proportional to a_1 and b_3 can generate a tree-level barrier, whose effect becomes active as T decreases due to the thermal mass contributions; (c) in the two-step scenario, the cross-quartic interaction proportional to a_2 generates a tree-level barrier between the pure singlet and Higgs (or mixed singlet-Higgs) vacuum; the effect of this barrier again depends on T due to the thermal mass contributions to the potential. In the present analysis, we retain only the gauge-invariant thermal mass contributions to the potential, so our parameter choices do not include the direct one-step transition (a). We defer an analysis of this case to future work.

In practice, we compute phase transition-relevant quantities using the CosmoTransitions package [60]. We obtain the critical temperature T_c at which the broken and unbroken phases are degenerate and the corresponding Higgs vev v_c . Both quantities are readily gauge invariant in the leading order high- T approximation. The condition for a strong first-order phase transition is approximately given by

$$\frac{v_c}{T_c} \gtrsim 1. \quad (\text{III.9})$$

IV. CONSTRAINTS ON PARAMETERS AND NUMERICAL RESULTS

In this section, we perform the numerical analysis. In the xSM, we have seven *a priori* unknown parameters in the tree-level potential – $a_1, a_2, b_3, b_4, \lambda, \mu^2, b_2$ – together with an undetermined singlet vev x_0 and a fixed Higgs vev $v_0 = 246$ GeV. Among all unknown parameters, two of them are expressed in terms of the scalar vacuum expectation values by two tadpole conditions in Eqs. (II.4). Thus, in our analysis, the μ^2, b_2 are expressed in terms of $a_1, a_2, b_3, b_4, \lambda, v_0$, and x_0 . Physical quantities can be calculated from the Higgs vev plus six *a priori* free input parameters. In the numerical analysis, we choose parameter sets randomly and calculate the corresponding SM-like Higgs mass, heavy resonance mass, the mixing angle between h_1 and h_2 and the heavy resonance production cross section. We require the SM-like Higgs mass to be 125 GeV and the mixing angle θ to satisfy the current Higgs signal strength measurement and electroweak precision observables (EWPO). Constraints on the mixing angle have been discussed in ref. [61], where it has shown that the

constraint from EWPO is more stringent than the bound given by Higgs measurements. The EWPO requires that the upper limit of $\sin^2 \theta$ varies from 0.12 to 0.04 when the resonance mass satisfies $250 \text{ GeV} < m_{h_2} < 950 \text{ GeV}$. The constraint of the global fit with single Higgs measurement, the 95% C.L. upper limit on $\sin^2 \theta$ is about 0.131 according to the previous work in Ref. [36]. Recently, a new measurement of m_W indicates a significant deviation of the W boson mass from the SM prediction based on the measured values of the other SM input parameters. The result can be translated into the theoretical EWPO predictions in the framework of the oblique parameters S, T and U. In the xSM, the oblique parameters receive additional contributions that depend on the singlet-like scalar mass m_2 and its mixing angle $\sin \theta$. Thus, one can find the allowed parameter region on $m_2 - \cos \theta$ plane determined by existing EWPO measurements as well as the new measurement of m_W . A detailed discussion appears in the Sec. IX C. Note that the new measurement indicates a very different parameter region from the previous measurement [61, 62] because of its deviation from the SM prediction. In what follows, we will utilize the EWPO constraints without including the new value of m_W for reasons discussed in detail in Sec. IX C.

For parameters with mass dimension one, x_0 , a_1 and b_3 , we require $|a_1| < 1 \text{ TeV}$ and $|b_3| < 1 \text{ TeV}$.

$$|a_1| < 1 \text{ TeV}, |b_3| < 1 \text{ TeV}, 10 \text{ GeV} \leq x_0 \leq 100 \text{ GeV}. \quad (\text{IV.1})$$

For dimensionless parameters, we set the ranges to be

$$0 < \lambda < 1, 0 < a_2 < 10, b_4 < 1 \quad (\text{IV.2})$$

following Ref. [59]. The randomly-chosen parameters in these ranges that satisfy SFOEWPT generally satisfy $a_2 \gtrsim 1$ and $0 < \lambda, b_4 < 1$. As compared to the other dimensionless parameters, we set a looser constraint on a_2 since its value has a more significant impact on the pathway to a SFOEWPT.

We study the collider phenomenology for the heavy singlet-like resonance production at the 14 TeV HL-LHC with $m_2 > 2m_1$, such that the decay of $h_2 \rightarrow h_1 h_1$ and $h_2 \rightarrow X_{SM} X_{SM}$ is allowed, where the X_{SM} stands for SM particle whose mass is less than $m_2/2$. Hence the branching ratio for $h_2 \rightarrow h_1 h_1$ is

$$BR(pp \rightarrow h_2 \rightarrow h_1 h_1) = \frac{\Gamma_{h_2 \rightarrow h_1 h_1}}{\Gamma_{h_2 \rightarrow h_1 h_1} + \sin^2 \theta \Gamma^{SM}(m_2)}. \quad (\text{IV.3})$$

We focus on the di-Higgs channel with $b\bar{b}\gamma\gamma$ final state and di-boson channel with four lepton final state. The cross-section of $pp \rightarrow h_2 \rightarrow h_1 h_1 \rightarrow b\bar{b}\gamma\gamma$ and $pp \rightarrow h_2 \rightarrow VV^* \rightarrow \ell\bar{\ell}\ell\bar{\ell}$ channels are calculated with narrow width approximation expressed in the following equations,

$$\sigma_{b\bar{b}\gamma\gamma} = \sigma_{pp \rightarrow h_2} \times BR(h_2 \rightarrow h_1 h_1) \times BR(h_1 \rightarrow b\bar{b}) \times BR(h_1 \rightarrow \gamma\gamma), \quad (\text{IV.4})$$

$$\sigma_{4\ell} = \sigma_{pp \rightarrow h_2} \times BR(h_2 \rightarrow ZZ) \times BR(ZZ \rightarrow 4\ell), \quad (\text{IV.5})$$

where the production cross-section, $\sigma_{pp \rightarrow h_2} = \sin^2 \theta \times \sigma_H(m_2)$, stands for the heavy resonance production. The $\sigma_H(m_{h_2})$ is the SM Higgs production cross section given by the CERN recommendation [63]. The total decay width of the heavy resonance h_2 is

$$\Gamma_{h_2} = \Gamma_{h_2 \rightarrow h_1 h_1} + \sin^2 \theta \Gamma_{h_1}(m_2), \quad (\text{IV.6})$$

where the $\Gamma_{h_1}(m_2)$ denotes the decay width function of standard model Higgs with a mass of m_2 . The decay width of $h_2 \rightarrow h_1 h_1$ in the equation above is

$$\Gamma_{h_2 \rightarrow h_1 h_1} = \frac{g_{211}^2 \sqrt{1 - \frac{4m_1^2}{m_2^2}}}{8\pi m_2}, \quad (\text{IV.7})$$

where the tri-Higgs coupling is obtained from the tree-level potential:

$$g_{211} = \frac{1}{4} [(a_1 + 2a_2 x_0) \cos^3 \theta + 4v_0 (a_2 - 3\lambda) \cos^2 \theta \sin \theta - 2(a_1 + 2a_2 x_0 - 2b_3 - 6b_4 x_0) \cos \theta \sin^2 \theta - 2a_2 v_0 \sin^3 \theta]. \quad (\text{IV.8})$$

In table I/table II, we list the benchmarks that maximize/minimize the $bb\gamma\gamma$ cross section for a given cross-section of 4ℓ channel.

Benchmark	$\sin \theta$	$g_{211}(\text{GeV})$	$m_s(\text{GeV})$	$a_1(\text{GeV})$	a_2	$b_3(\text{GeV})$	b_4	λ	$v_x(\text{GeV})$	$\sigma_{4\ell} (pb)$	$\sigma_{bb\gamma\gamma} (pb)$
B1	0.221	89	257	-652	2.94	-488	0.370	0.141	95.4	1.56×10^{-4}	1.06×10^{-3}
B2	0.228	120	301	-801	4.14	-832	0.303	0.170	80.7	1.28×10^{-4}	9.62×10^{-4}
B3	-0.216	-126	349	-226	4.71	819	0.793	0.168	43.6	1.39×10^{-4}	8.63×10^{-4}
B4	-0.197	-141	401	-387	5.52	817	0.804	0.177	55.8	1.11×10^{-4}	5.95×10^{-4}
B5	-0.184	-152	448	-548	6.33	982	0.357	0.183	64.8	7.66×10^{-5}	3.53×10^{-4}
B6	-0.178	-163	497	-829	7.10	981	0.502	0.191	81.7	5.50×10^{-5}	2.00×10^{-4}
B7	0.147	119	550	-881	6.78	-929	0.281	0.187	40.0	3.21×10^{-5}	6.09×10^{-5}
B8	0.134	127	598	-937	7.70	-918	0.714	0.184	36.9	1.86×10^{-5}	3.41×10^{-5}
B9	0.118	130	645	-958	8.75	-950	0.554	0.176	32.8	1.04×10^{-5}	1.88×10^{-5}
B10	0.106	132	696	-980	9.81	-857	0.332	0.172	29.4	5.92×10^{-6}	9.977×10^{-6}
B11	0.095	120	753	-952	9.82	923	0.696	0.164	26.8	3.45×10^{-6}	4.37×10^{-6}

TABLE I: Benchmark parameter choices that maximize the $bb\gamma\gamma$ channel cross section when the 4ℓ cross section is fixed.

Benchmark	$\sin \theta$	$g_{211}(\text{GeV})$	$m_s(\text{GeV})$	$a_1(\text{GeV})$	a_2	$b_3(\text{GeV})$	b_4	λ	$v_x(\text{GeV})$	$\sigma_{4\ell} (pb)$	$\sigma_{bb\gamma\gamma} (pb)$
B1	0.133	10	258	-197	0.91	236	0.750	0.139	78.4	1.57×10^{-4}	2.38×10^{-5}
B2	0.129	10	298	-261	1.06	414	0.434	0.138	86.8	1.25×10^{-4}	2.75×10^{-5}
B3	0.129	5	349	-279	0.98	786	0.219	0.140	85.8	1.37×10^{-4}	4.23×10^{-6}
B4	0.128	9	401	-402	1.38	973	0.174	0.148	91.5	1.09×10^{-4}	7.11×10^{-6}
B5	0.136	19	453	-320	2.02	986	0.510	0.165	27.9	8.24×10^{-5}	1.13×10^{-5}
B6	0.135	27	504	-410	2.73	813	0.793	0.157	27.3	5.40×10^{-5}	9.51×10^{-6}
B7	0.125	32	547	-457	3.33	946	0.267	0.157	25.6	3.31×10^{-5}	6.92×10^{-6}
B8	0.116	40	602	-528	4.29	860	0.251	0.165	23.7	1.86×10^{-5}	4.52×10^{-6}
B9	0.103	49	647	-570	5.32	923	0.885	0.164	21.9	1.04×10^{-5}	3.55×10^{-6}
B10	0.095	53	704	-617	6.31	959	0.227	0.155	19.8	5.84×10^{-6}	1.95×10^{-6}
B11	0.087	68	752	-688	7.92	818	0.477	0.159	19.1	3.38×10^{-6}	1.70×10^{-6}

TABLE II: Benchmark parameter choices that minimize the $bb\gamma\gamma$ channel cross section when the 4ℓ cross section is fixed.

The scan result is illustrated in Fig. 1, where we plot the cross section for $pp \rightarrow h_2 \rightarrow h_1 h_1 \rightarrow bb\gamma\gamma$ and $pp \rightarrow h_2 \rightarrow VV^* \rightarrow 4\ell$ to show their correlation. In the next section, we will study the current bounds on the two channels at LHC.

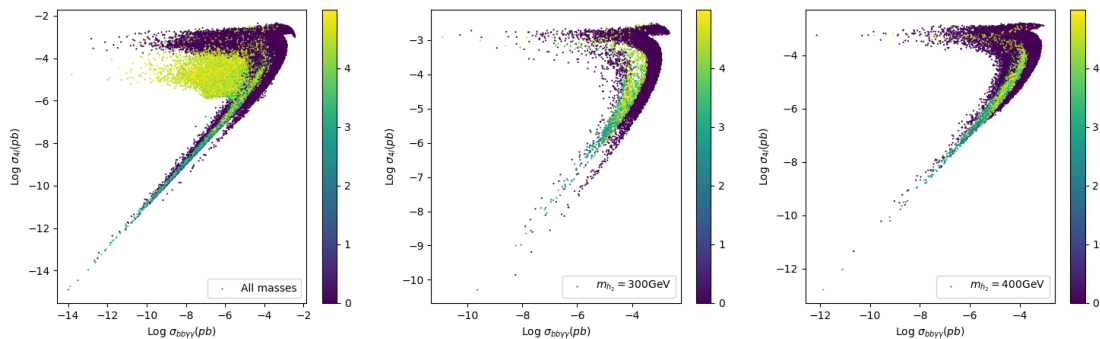


FIG. 1: Distribution of logarithm of the cross section of $bb\bar{\gamma}\gamma$ and $4l$ channels. The color stands for first-order EWPT strength as defined in Eq. (III.9). The left panel shows all results with m_{h_2} varying from 260 GeV to 800 GeV. The mass in the middle and right plots equals 300 GeV and 400 GeV, respectively.

V. SIMULATION OF SIGNAL AND BACKGROUND DISTRIBUTIONS

The strategy of signal and background simulation is as follows: two 13 TeV ATLAS analyses channels $pp \rightarrow h_2 \rightarrow h_1 h_1$ [26] and $pp \rightarrow h_2 \rightarrow VV^*$ [22] where $h_1 \rightarrow b\bar{b}/\gamma\gamma$ and $V \rightarrow \ell\bar{\ell}$, are taken as references for event selection and background distribution. A factor of 1.18 is applied to backgrounds to count for collision energy upgrade from 13 TeV to 14 TeV, as commonly used in ATLAS prospective studies. The signal processes at 14 TeV center-of-mass energy are generated for heavy singlet-like mass states, whose mass ranges from 270 GeV to 800 GeV in steps of 50 GeV. The simulation process is presented briefly in the following, with more details of signal cut-flow being given in Appendix IX.

In the $b\bar{b}\gamma\gamma$ channel as described in reference [26], the four-body invariant mass $m_{b\bar{b}\gamma\gamma}$ is used as the discriminating variable. Events are categorized into four signal-enriched regions according to number of b-tagged jets as well as loose and tight event selection criteria: "1-btag loose", "2-btag loose", "1-btag tight" and "2-btag tight". The "1-btag" and "2-btag" means that at least one and two jets should be recognized as b-jets. Acceptances after passing signal-enriched region are in good agreement with the reference analysis, as shown in Table III in Appendix IX. For background, the $m_{b\bar{b}\gamma\gamma}$ distributions from reference analysis are extracted. An exponential function is used to fit the $m_{b\bar{b}\gamma\gamma}$ curve in each signal-enriched region, and then use the fitted function to generate $m_{b\bar{b}\gamma\gamma}$ distributions according to 3 ab^{-1} luminosity. An $\pm 2\%$ error value is assigned as luminosity calculation uncertainty. The $b\bar{b}\gamma\gamma$ distributions of signal and background are shown in Fig. 2. The normalizations of signals on the plots are arbitrary.

In the $VV \rightarrow 4\ell$ channel, as described in the reference [22], the four-body invariant mass $m_{4\ell}$ is used as the discriminating variable. Events have to pass signal-enriched region selection, which is given with more details in Appendix IX section B). Signal efficiency is in reasonable agreement with the reference analysis. A similar approach as $b\bar{b}\gamma\gamma$ analysis is used to simulate background distributions. Fig. 3 shows the $m_{4\ell}$ distributions of signal and background processes. The normalization of signals on the plots are arbitrary.

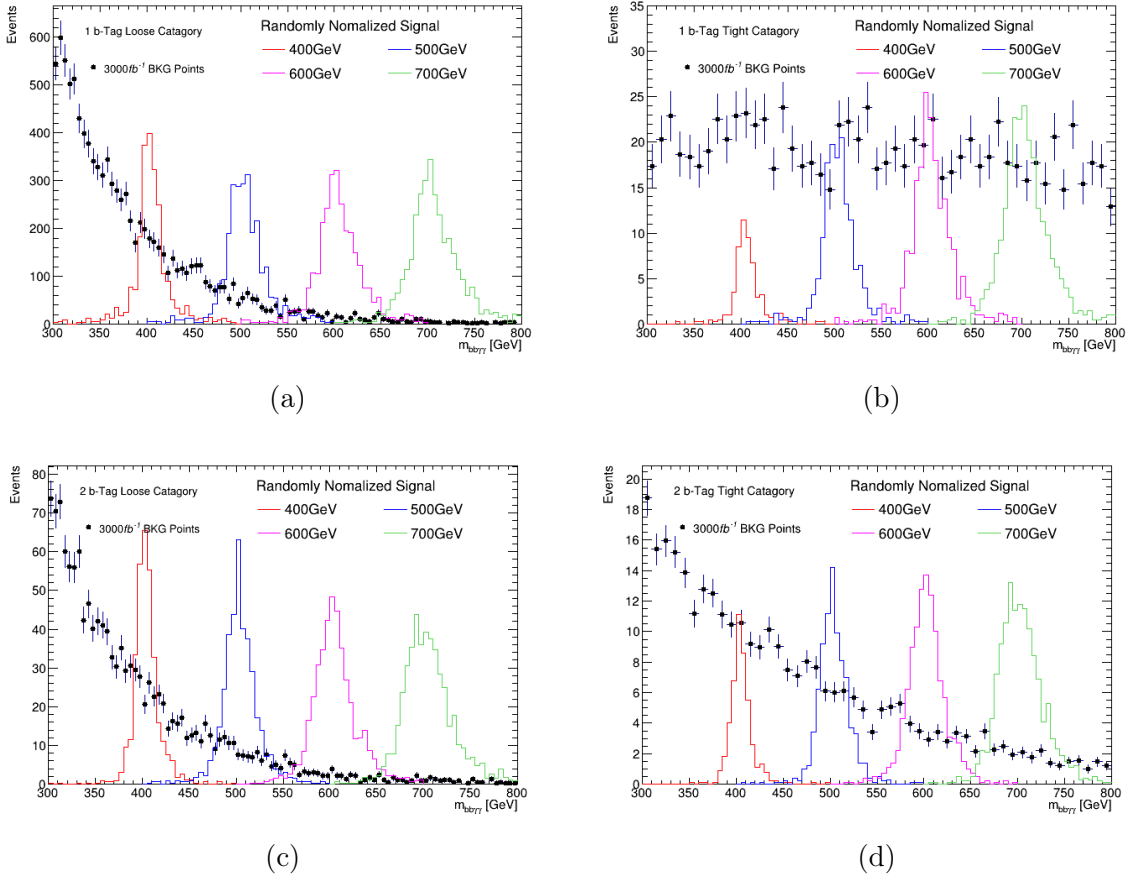


FIG. 2: The $m_{bb\gamma\gamma}$ distributions of the $bb\gamma\gamma$ channel analysis, in four signal-enriched regions: "1-btag loose", "2-btag loose", "1-btag tight" and "2-btag tight", respectively. The normalization of signal processes are arbitrary.

VI. SENSITIVITY AND EXCLUSION LIMITS ANALYSIS

As has been well-studied in earlier work and confirmed in the present analysis, there exists a wide range of xSM parameters compatible with a SFOEWPT. As shown in Fig. 1, the SFOEWPT-compatible choices can lead to non-trivial correlations between $\sigma_{h_2 \rightarrow VV \rightarrow 4\ell}$ and $\sigma_{h_2 \rightarrow h_1 h_1 \rightarrow bb\gamma\gamma}$, particularly for the region for smaller cross sections. On the other hand, for the larger values of $\sigma_{h_2 \rightarrow VV \rightarrow 4\ell}$ this correlation evaporates.

In order to carry out a systematic analysis of the LHC reach in this parameter space, we adopt the following procedure. For each resonance mass point, a set of $\sigma_{h_2 \rightarrow VV \rightarrow 4\ell}$ points are selected, which cover the full range and distribute uniformly. For each fixed $\sigma_{h_2 \rightarrow VV \rightarrow 4\ell}$ point, we choose two parameter sets, corresponding to the maximum and minimum values of $\sigma_{h_2 \rightarrow h_1 h_1 \rightarrow bb\gamma\gamma}$. Thus, for each mass point, overall 10~15 $\sigma_{h_2 \rightarrow VV \rightarrow 4\ell}$ points are selected which results from 20~30 points on the $\sigma_{h_2 \rightarrow VV \rightarrow 4\ell}$ and $\sigma_{h_2 \rightarrow h_1 h_1 \rightarrow bb\gamma\gamma}$ plane.

Fig. 4 shows the prospective discovery significance for HL-LHC with 3 ab^{-1} integrated luminosity, from the $VV \rightarrow 4\ell$ channel, and from the $h_1 h_1 \rightarrow bb\gamma\gamma$ channel with maximum and minimum cross-section, respectively. The $h_1 h_1 \rightarrow bb\gamma\gamma$ channel with a maximum cross-section (red region in the left plot) has, on average larger sensitivity than the minimum

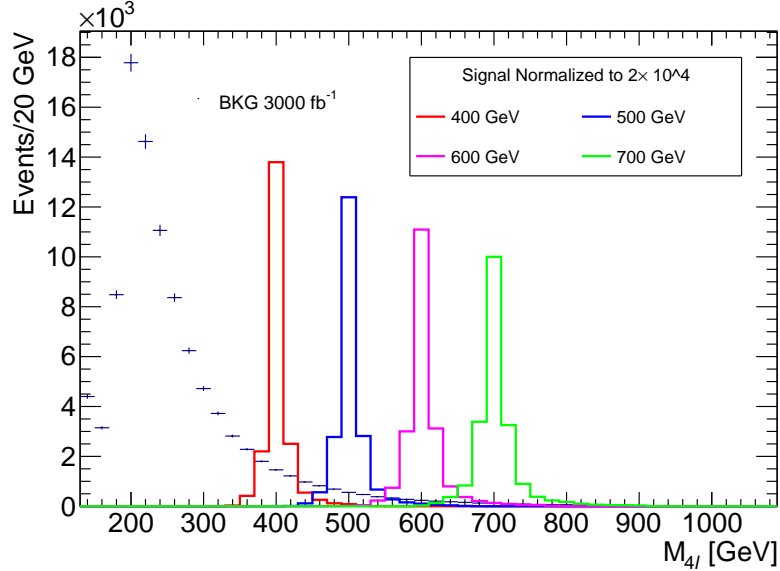


FIG. 3: Distribution of reconstructed four charged leptons for $h_2 \rightarrow ZZ \rightarrow 4\ell$. The number of signal events is normalized to 2×10^4 . The number of background events is normalized with the integrated luminosity of $3ab^{-1}$.

cross-section (red region in the right plot). Compared to the $h_1h_1 \rightarrow bb\gamma\gamma$, the $VV \rightarrow 4\ell$ channel (blue region) has better sensitivity, particularly for higher mass resonance signals. The $VV \rightarrow 4\ell$ channel can reach to 5-sigma discovery significance over a wide mass range from 300 GeV to 750 GeV.

It is worth emphasizing that the $VV \rightarrow 4\ell$ sensitivity is generic for any heavy Higgs that has a VV decay mode and is not specific to the xSM model. Thus, the observation of this mode at a given mass with the significance indicated would be compatible with the SFOEWPT in the xSM but not conclusive. Conversely, the non-observation of this mode would preclude the SFOEWPT-viable xSM with a heavy resonance in a significant portion of parameter space.

On the other hand, the $h_1h_1 \rightarrow bb\gamma\gamma$ channel would provide a diagnostic probe with some sensitivity up to around 500 GeV. In terms of exclusions corresponding to the 2-sigma line on the plots, both $h_1h_1 \rightarrow bb\gamma\gamma$ and $VV \rightarrow 4\ell$ channels have some sensitivity. In order to enhance the analysis sensitivity, results from the two channels are therefore combined. The combined discovery significance is shown in Fig. 5. More than half of the considered phase space points can be excluded at HL-LHC with $3 ab^{-1}$ integrated luminosity. On the other hand, there are also points below the 1σ line on the plots, which can be further investigated at future colliders.

With these results in mind, one can anticipate several possible experimental outcomes:

- (i) Most optimistically, both modes with a resonance mass below ~ 400 GeV (Fig. 4, left panel) are observed: there would be strong evidence for the SFOEWPT-viable xSM.
- (ii) Neither channel is observed at the HL-LHC: the SFOEWPT-viable xSM might still be realized in nature, but the parameters would correspond to the regions of the plots below the 2σ lines.

- (iii) The $VV \rightarrow 4\ell$ is observed but the $h_1 h_1 \rightarrow bb\gamma\gamma$ is not: the existence of a heavy resonance compatible with the SFOEWPT-xSM would be established but a future more sensitive search for the $h_1 h_1 \rightarrow bb\gamma\gamma$ would be needed.
- (iv) The $h_1 h_1 \rightarrow bb\gamma\gamma$ is observed but the $VV \rightarrow 4\ell$ is not: there would exist strong evidence for the SFOEWPT-viable xSM, but a future, more sensitive search for the $VV \rightarrow 4\ell$ channel would be needed to probe the parameter space below the 2σ line in order to be conclusive.

Note that for each possible outcome, one would need to perform an updated parameter xSM parameter scan that takes into account the various experimental results.

The combined results are interpreted as exclusion regions in the g_{211} and $\sin\theta$ parameters, as shown in Fig. 6 for a 400 GeV resonance mass. From left to right, these plots show the parameter space allowed by, respectively, a first-order EWPT, SFOEWPT, and the HL-LHC (if the future experiment were not to find the resonant diboson decay from the heavy Higgs). The middle panel indicates that, for parameters yielding a SFOEWPT, the distribution of $g_{211} - \sin\theta$ is asymmetric, and a positive θ with a positive g_{211} tends to give a stronger first-order EWPT. The reason is that most of the points in the middle panel correspond to a 2-step EWPT, where a positive a_2 is necessary to generate a barrier for a 2-step transition and, hence, will be more likely to induce a positive g_{211} .

In the third panel, the points that are within 5σ signal significance are presented. Comparing with the middle panel, one observes that the parameter space with large $|g_{211}|$ and large $|\sin\theta|$ is more likely to be detected, where $|g_{211}| > 40$ GeV with $\sin\theta > 0.1$ and $|g_{211}| > 40$ GeV with $\sin\theta < -0.05$ are able to be discovered by the HL-LHC.

On the other hand, if HL-LHC does not observe a signal, two interesting features can be observed from the plot in the rightmost panel. First, the asymmetry for positive and negative $\sin\theta$ indicates that the signs of $\sin\theta$ and g_{211} are correlated, *i.e.* a positive $\sin\theta$ indicates a positive g_{211} and vice versa. Second, for a negative $\sin\theta$, the value of g_{211} and $\sin\theta$ are strongly correlated, as one can see from the plot, the allowed parameter space in this region tends to be a narrow band. Since the resonant, $h_2 \rightarrow h_1 h_1$ and $h_2 \rightarrow VV$ ($V = Z, W$) rates depend on $\sin^2\theta$, it is not possible to test the sign correlation solely using the resonant di-boson production processes studied here. Processes sensitive to the other couplings, such as g_{221} , may provide additional, complementary information as needed for such a test.

We would like to point out here that the independent measurement of the sign of $\sin\theta$ is not an easy task, and one cannot determine the sign of $\sin\theta$ with solely the couplings between h_2 and SM fermions or vector bosons, because in this case each propagator of h_2 present in a diagram must contribute to 2 powers of $\sin\theta$ erasing the sign information. What's worse, even if including the g_{211} does not help to disentangle the sign effect if nature is realized with xSM with SFOEWPT as indicated by the first feature. In this case, the only hope might be to rely on a global fit that includes physical processes that are sensitive to all the scalar couplings to determine the sign of $\sin\theta$.

VII. CONCLUSION

Exploring the thermal history of electroweak symmetry breaking is an important effort in its own right and may yield clues to solving the baryogenesis problem through EWBG. This scenario requires a SFOEWPT as a pre-condition for generation of the CPV asymmetries that ultimately yield the baryon asymmetry. In the SM, EWSB occurs through a cross-over

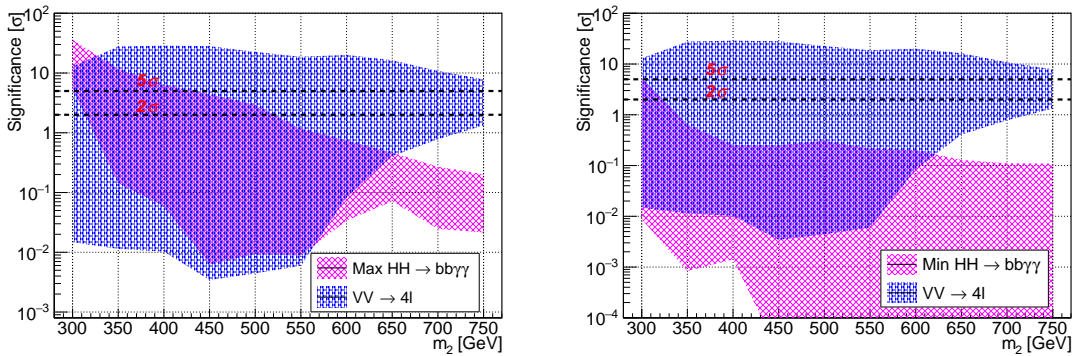


FIG. 4: Prospective discovery/exclusion reach for HL-LHC with $3 ab^{-1}$. Horizontal and vertical axes give heavy scalar mass and significance, respectively. Red points in the left (right) panels indicate range of maximum (minimum) $\sigma_{h_1 h_1 \rightarrow bb\gamma\gamma}$ as one varies over the range of $\sigma_{VV \rightarrow 4l}$. The significance for the latter is indicated by the blue points. For a fixed M_S , $\sigma_{VV \rightarrow 4l}$ depends mainly on $\sin\theta$ mainly. All points satisfy the requirement of SFOEWPT.

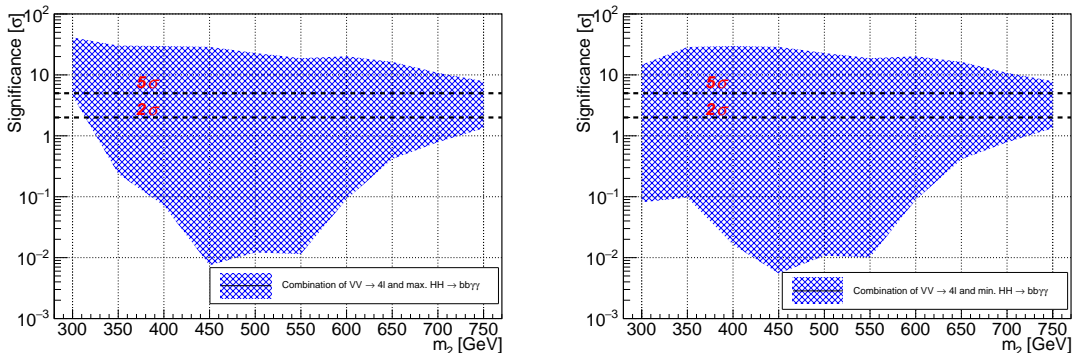


FIG. 5: Prospective discovery/exclusion reach for HL-LHC with $3 ab^{-1}$ from the combination of two channels: (1) the $VV \rightarrow 4l$ channel, and (2) $h_1 h_1 \rightarrow bb\gamma\gamma$ channel with maximum cross section (left panel) and with minimum cross section (right panel).

transition. However, the Higgs portal interactions in the xSM can generate a SFOEWPT for suitable choices of model parameters. As is well-known, an effective way to probe the Higgs portal interactions is the heavy scalar resonance search via di-Higgs channel.

In this work, we have analyzed the complementarity between the searches for resonant di-Higgs production and a heavy, SM-like Higgs that decays into four leptons. In the generic xSM, mixing between the singlet scalar and neutral component of the Higgs doublet yields a new singlet-like state having both decay channels if sufficiently heavy. For the di-Higgs channel, we have considered in particular the $bb\gamma\gamma$ final state. We show that the $bb\gamma\gamma$ channel is able to explore the low mass region with $m_2 \lesssim 450$ GeV effectively and the $4l$ channel is more suitable for the high mass region with $m_2 \gtrsim 500$ GeV. In terms of exclusion, one is able to exclude the portion of SFOEWPT parameter space by taking advantage of the combination of $bb\gamma\gamma$ and $4l$ channels over roughly $m_2 \lesssim 780$ GeV at the 14 TeV HL-LHC

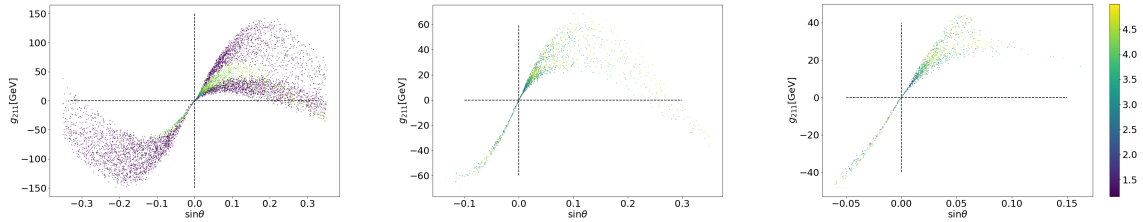


FIG. 6: For 400 GeV resonance mass, the parameter space as a function of g_{211} and $\sin\theta$ allowed by the first-order EWPT in the current situation (left panel), SFOEWPT (middle panel), and non-observation at the HL-LHC with $3 ab^{-1}$ from this study (right panel).

with luminosity $3ab^{-1}$. Moreover, the combination of both channels provides an important diagnostic probe of the SFOEWPT-viable xSM. However, signal events associated with minimal $b\bar{b}\gamma\gamma$ cross section are difficult to exclude at the HL-LHC, pointing to the need for a future collider with higher energy to obtain a comprehensive probe (see, *e.g.*, Refs. [13, 16]).

VIII. ACKNOWLEDGEMENT

SA, MJRM and WZ are supported in part under National Natural Science Foundation of China grant No. 11975150. H.-L.L. is supported by F.R.S.-FNRS through the IISN convention "Theory of Fundamental Interactions" (N: 4.4517.08).

IX. APPENDIX

In this section, the details of the simulation will be listed. The first subsection will discuss simulations in $b\bar{b}\gamma\gamma$ channel and simulations in 4ℓ channel in the second subsection.

A. $b\bar{b}\gamma\gamma$ channel simulation

We perform a generation of a signal process $pp \rightarrow h_2 \rightarrow h_1 h_1 \rightarrow b\bar{b}\gamma\gamma$ by utilizing MadGraph5 [64] in parton level and use Pythia8 [65] to simulate the parton shower process followed by a detector simulating software Delphes3 [66] to simulate the detector response of this process at LHC. In this section, we will follow the ATLAS analysis in Ref. [26] and reproduce the cutflow efficiency compared with the experimental data.

In the detector simulation, photon candidates must satisfy isolation criteria of $\Delta R \leq 0.2$ for both calorimeter- and track-based isolation. In track-based isolation, the transverse momentum within the cone (p_T^{iso}) counts only the tracks with $p_T > 1$ GeV. Jets are reconstructed using anti- k_t clustering algorithm [67] with a radius parameter set to be $R = 0.4$ and are required to satisfy $|\eta| < 2.5$ and $p_T > 25$ GeV. In addition, the efficiency for a b-quark jet to pass the b -tagging requirement is set to be a constant equal to 70% [68] approximately.

The selection is simplified according to Ref. [26]:

- Events are required to have at least two photons and two jets with one or two jets recognized as b-jet(s). Any event containing more than two b-jets is rejected.
- The invariant mass of two photon with the highest p_T should satisfy $105 \text{ GeV} < m_{\gamma\gamma} < 160 \text{ GeV}$.
- For each photon, it is required to have $E_T/m_{\gamma\gamma} > 0.35$ and 0.25 respectively.
- Four signal regions are defined based on the highest- p_T and next-highest p_T (They are called "Cen Jets" in Table. III). If $p_T^1 > 40\text{GeV}$ and $p_T^2 > 25\text{GeV}$, the signal is labeled with "loose". If $p_T^1 > 100\text{GeV}$ and $p_T^2 > 30\text{GeV}$, the signal is labeled "tight". Combining with the b-jet number, signal events are classified to four regions, which are "1-btag loose", "1-btag tight", "2-btag loose" and "2-btag tight".
- For tight (loose) signal regions, the diphoton invariant mass is required to be $125 \text{ GeV} \pm 4.3(4.7) \text{ GeV}$.
- The dijet system is rescaled by a factor of m_H/m_{jj} .
- Loose selection is used for resonances with $m_X \leq 400 \text{ GeV}$ and the tight selection for resonances with $m_X \geq 400 \text{ GeV}$. For tight (loose) selection, we require $335 \text{ GeV} < m_{\gamma\gamma jj} < 1140 \text{ GeV}$ ($245 \text{ GeV} < m_{\gamma\gamma jj} < 610 \text{ GeV}$).
- For events that pass the selection above, we obtain their $m_{bb\gamma\gamma}$ distribution.

	$m_{\gamma\gamma}$	2 Cen Jets	b-tagging	bjet pT	m_{bb}	$E_T/m_{\gamma\gamma}$
Exp(300GeV 1-btag)	37.6%	27.80%	11.8%	10.8%	5.9%	5.6%
Sim(300GeV 1-btag)	37.6%	27.9%	12.65%	9.56%	5.52%	5.39%
Exp(300GeV 2-btag)	37.6%	27.8%	8.1%	7.9%	6.8%	6.4%
Sim(300GeV 2-btag)	37.6%	27.9%	7.63%	7.09%	5.84%	5.82%
Exp(400GeV 1-btag)	40.2%	32.8%	14.3%	5.5%	2.5%	2.4%
Sim(400GeV 1-btag)	40.2%	32.7%	13.44%	5.42%	1.98%	1.98%
Exp(400GeV 2-btag)	40.2%	32.8%	10.3%	4.3%	3.6%	3.4%
Sim(400GeV 2-btag)	40.2%	32.7%	12.05%	4.85%	3.70%	3.70%

TABLE III: Cutflows for higgs production at LHC with $\sqrt{s} = 1.3 \text{ TeV}$, $m_{h_2} = 300/400 \text{ GeV}$, $\mathcal{L} = 250 \text{ fb}^{-1}$. The Exp-line shows the experimental result in ref [26]. The Sim-line shows the simulation result.

B. $ZZ \rightarrow 4\ell$ channel simulation and selection

We generate the parton level signal events $pp \rightarrow h_2 \rightarrow ZZ \rightarrow \ell^+\ell^-\ell^+\ell^-$ with MadGraph5 [64], then showering with Pythia8 [65] and simulate the detector effect with Delphes3 [66]. We follow the ATLAS analysis in Ref. [22], and reproduce similar signal and background efficiencies in that paper. The analysis cut flow is described as followings:

- Select the events with two same-flavor opposite-sign lepton pairs. The reconstructed electron (muon) must have $p_T > 7(5) \text{ GeV}$ and $|\eta| < 2.47(2.7)$.

- For lepton pairs, we denote the invariant mass of the pair closer to Z mass as m_{12} and that of the other pair as m_{34} . We demand that m_{12} and m_{34} satisfying the following cuts:

$$\begin{aligned}
& 50 \text{ GeV} < m_{12} < 106 \text{ GeV} \\
& m_{34} < 116 \text{ GeV} \\
& m_{34} > \begin{cases} 12 \text{ GeV} & m_{4\ell} \leq 140 \text{ GeV} \\ 12 + 50 \frac{m_{4\ell} - 140}{190 - 140} & 140 \text{ GeV} < m_{4\ell} < 190 \text{ GeV} \\ 50 \text{ GeV} & m_{4\ell} \geq 190 \text{ GeV} \end{cases} \quad (\text{IX.1})
\end{aligned}$$

- We also require that leptons are separated with each other by $\Delta R > 0.1$ if they are the same flavor, and $\Delta R > 0.2$ otherwise.
- For 4μ and $4e$ events, we veto the events containing opposite-sign lepton pairs with $m_{\ell\ell} < 5 \text{ GeV}$.
- We implement the cut on the track-isolation discriminant as the sum of the transverse momenta of tracks within $\Delta R = 0.3$ (0.2) of the muon (electron) candidate excluding the lepton track, divided by the p_T of the lepton. Such discriminants are required to be smaller than 0.15.

Compared to Ref. [22], we did not impose the calorimeter-based isolation requirement because they are technically difficult to implement in the Delphes. In practice, we find that the major effect on the signal efficiencies is from the detector efficiencies for leptons, and with the above cuts we are already able to obtain signal efficiencies reasonably close to those in the ATLAS paper [22]. In table. IV, we illustrate the effectiveness of our simulation by showing the comparison of signal efficiencies for different lepton channels for a fixed benchmark point $m_2 = 600 \text{ GeV}$, we only compare the final efficiencies because the efficiencies for the intermediate cuts are inaccessible in the experimental paper.

	Sim (600 GeV)	Exp (600 GeV)
4μ	42.2%	48%
$4e$	63.4%	64%
$2\mu 2e$	51.7%	57%

TABLE IV: Signal efficiencies for different lepton channels of the process the $h_2 \rightarrow ZZ \rightarrow 4\ell$, the Exp numbers are obtained from Ref. [22].

C. Comments on the constraint from electroweak precision observables (EWPO)

xSM can influence EWPO in two ways: rescaling couplings between the SM-like Higgs to SM particles and generating new diagrams involving the single-like Higgs. When parameterizing theoretical predictions of EWPO in the framework of the oblique parameters S, T and U [69, 70], the shifted oblique parameters in the xSM can be uniquely determined by

the two physical parameters: the mixing angle θ and the mass of the singlet-like Higgs m_2 , which can be expressed in the following formula,

$$\Delta\mathcal{O} = (\cos^2\theta - 1)\mathcal{O}^{\text{SM}}(m_1) + \sin^2\theta\mathcal{O}^{\text{SM}}(m_2) = \sin^2\theta [\mathcal{O}^{\text{SM}}(m_2) - \mathcal{O}^{\text{SM}}(m_1)], \quad (\text{IX.2})$$

where \mathcal{O} can be either S, T or U , and $\mathcal{O}^{\text{SM}}(m_2)$ are the SM expression for \mathcal{O} if the Higgs mass were to be m_2 . Therefore a constraint on the $\cos\theta - m_2$ plane can be derived by constructing the χ^2 with the predicted oblique observables and the experimental data. In our previous work [36], we used the global fitted center values, uncertainties, and correlations for these oblique parameters from the Gfitter group [71] and obtained a lower bound on $\cos\theta$ as a function of m_2 . However, the recently updated measurement of m_W from the CDF collaboration [72] exhibits a significant deviation from the SM prediction, which indicates a qualitative change in the EWPO constraint for xSM.

To illustrate the potential influence of such a new m_W measurement on the EWPO constraint for xSM, we follow the recent global fit result by the HEPfit group [73], where they combine the measurements from LEP2, LHC and Tevatron including the most recent CDFII results to give a new “world average” of W mass as:

$$m_W = 80.4133 \pm 0.0080 \text{ (0.015) GeV}, \quad (\text{IX.3})$$

where the number in the parenthesis represents an inflated error for a conservative average. From this updated value of m_W , authors in Ref. [73] derive four sets of constraints on the S, T , and U parameters assuming whether one uses the conservative average or not and whether one sets $U = 0$ or not. As an example, we plot the allowed parameter space at 95% confidence level (CL) in the $\cos\theta - m_2$ plane in the blue region in Fig. 7 assuming $U = 0$ and m_W taking the conservative average, which corresponds to the following bounds and correlations matrix on the S and T parameters:

$$\Delta S = 0.086 \pm 0.077, \quad \Delta T = 0.177 \pm 0.070, \quad (\text{IX.4})$$

$$\rho = \begin{pmatrix} 1 & 0.89 \\ 0.89 & 1 \end{pmatrix}. \quad (\text{IX.5})$$

One can find that the allowed parameter space tends to have a very small m_2 such that the diHiggs decay channel is not available. This is expected, since the updated W boson mass from CDFII indicates a relatively large violation of custodial symmetry, while xSM scalar potential does not explicitly break the custodial symmetry, as a consequence, the new physics contribution to the custodial symmetry breaking starts at one-loop receiving a loop factor suppression, to compensate such a suppression one needs a relatively small singlet-like Higgs mass. However, we need to emphasize here that the above global analysis heavily depends on the method used for combining the W mass measurements from different experiments, given that the newly measured m_W has a significant discrepancy compared with all the previous measurements, the ordinary averaging method assuming correlated Gaussian uncertainties may not be appropriate anymore, and the community has not reached a common agreement on the interpretation of the experimental results yet.

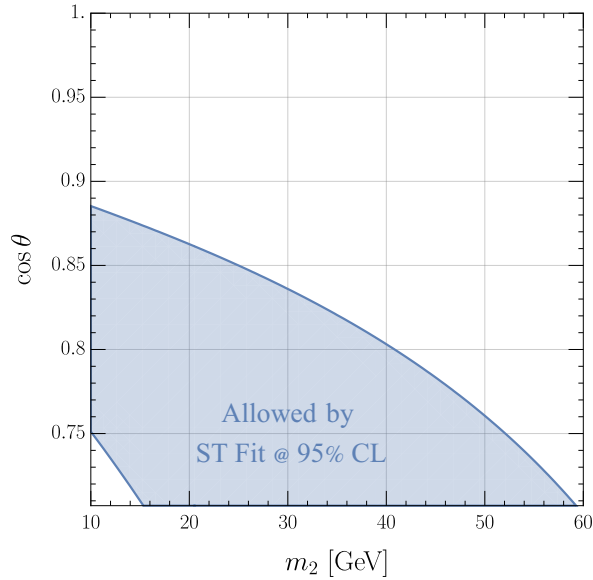


FIG. 7: The allowed parameter space at 95% CL for xSM using the global fit from Ref. [73] assuming $U = 0$ and M_W with conservative average. The vertical axis start from $\theta = \pi/4$, above which the mass eigenstate h_1 gets more contribution from the neutral part in the Higgs doublet thus corresponding to the SM-like Higgs.

-
- [1] G. Aad et al. (ATLAS), *Phys. Lett. B* **716**, 1 (2012), arXiv:1207.7214 [hep-ex].
 - [2] S. Chatrchyan et al. (CMS), *Phys. Lett. B* **716**, 30 (2012), arXiv:1207.7235 [hep-ex].
 - [3] P. A. R. Ade et al. (Planck), *Astron. Astrophys.* **571**, A16 (2014), arXiv:1303.5076 [astro-ph.CO].
 - [4] V. A. Kuzmin, V. A. Rubakov, and M. E. Shaposhnikov, *Phys. Lett. B* **155**, 36 (1985).
 - [5] M. E. Shaposhnikov, *JETP Lett.* **44**, 465 (1986).
 - [6] M. E. Shaposhnikov, *Nucl. Phys. B* **287**, 757 (1987).
 - [7] A. G. Cohen, D. B. Kaplan, and A. E. Nelson, *Ann. Rev. Nucl. Part. Sci.* **43**, 27 (1993), arXiv:hep-ph/9302210.
 - [8] D. E. Morrissey and M. J. Ramsey-Musolf, *New J. Phys.* **14**, 125003 (2012), arXiv:1206.2942 [hep-ph].
 - [9] A. D. Sakharov, *Pisma Zh. Eksp. Teor. Fiz.* **5**, 32 (1967).
 - [10] K. Kajantie, M. Laine, K. Rummukainen, and M. E. Shaposhnikov, *Nucl. Phys. B* **493**, 413 (1997), arXiv:hep-lat/9612006.
 - [11] F. R. Klinkhamer and N. S. Manton, *Phys. Rev. D* **30**, 2212 (1984).
 - [12] K. Kajantie, M. Laine, K. Rummukainen, and M. E. Shaposhnikov, *Phys. Rev. Lett.* **77**, 2887 (1996), arXiv:hep-ph/9605288.
 - [13] M. J. Ramsey-Musolf, *JHEP* **09**, 179 (2020), arXiv:1912.07189 [hep-ph].
 - [14] D. O'Connell, M. J. Ramsey-Musolf, and M. B. Wise, *Phys. Rev. D* **75**, 037701 (2007), arXiv:hep-ph/0611014.
 - [15] S. Profumo, M. J. Ramsey-Musolf, and G. Shaughnessy, *JHEP* **08**, 010 (2007), arXiv:0705.2425

- [hep-ph].
- [16] A. V. Kotwal, M. J. Ramsey-Musolf, J. M. No, and P. Winslow, *Phys. Rev. D* **94**, 035022 (2016), [arXiv:1605.06123 \[hep-ph\]](#).
 - [17] K. Hashino, M. Kakizaki, S. Kanemura, P. Ko, and T. Matsui, *Phys. Lett. B* **766**, 49 (2017), [arXiv:1609.00297 \[hep-ph\]](#).
 - [18] M. Aaboud *et al.* (ATLAS), *JHEP* **01**, 030 (2019), [arXiv:1804.06174 \[hep-ex\]](#).
 - [19] A. M. Sirunyan *et al.* (CMS), *JHEP* **08**, 152 (2018), [arXiv:1806.03548 \[hep-ex\]](#).
 - [20] M. Aaboud *et al.* (ATLAS), *JHEP* **04**, 092 (2019), [arXiv:1811.04671 \[hep-ex\]](#).
 - [21] A. M. Sirunyan *et al.* (CMS), *JHEP* **01**, 054 (2018), [arXiv:1708.04188 \[hep-ex\]](#).
 - [22] M. Aaboud *et al.* (ATLAS), *Eur. Phys. J. C* **78**, 293 (2018), [arXiv:1712.06386 \[hep-ex\]](#).
 - [23] M. Aaboud *et al.* (ATLAS), *JHEP* **05**, 124 (2019), [arXiv:1811.11028 \[hep-ex\]](#).
 - [24] M. Aaboud *et al.* (ATLAS), *Phys. Rev. Lett.* **121**, 191801 (2018), [Erratum: *Phys.Rev.Lett.* **122**, 089901 (2019)], [arXiv:1808.00336 \[hep-ex\]](#).
 - [25] A. M. Sirunyan *et al.* (CMS), *Phys. Lett. B* **778**, 101 (2018), [arXiv:1707.02909 \[hep-ex\]](#).
 - [26] M. Aaboud *et al.* (ATLAS), *JHEP* **11**, 040 (2018), [arXiv:1807.04873 \[hep-ex\]](#).
 - [27] A. M. Sirunyan *et al.* (CMS), *Phys. Lett. B* **788**, 7 (2019), [arXiv:1806.00408 \[hep-ex\]](#).
 - [28] G. Aad *et al.* (ATLAS), *Eur. Phys. J. C* **80**, 1165 (2020), [arXiv:2004.14636 \[hep-ex\]](#).
 - [29] M. Aaboud *et al.* (ATLAS), *JHEP* **03**, 042 (2018), [arXiv:1710.07235 \[hep-ex\]](#).
 - [30] M. Aaboud *et al.* (ATLAS), *JHEP* **09**, 173 (2016), [arXiv:1606.04833 \[hep-ex\]](#).
 - [31] M. Aaboud *et al.* (ATLAS), *Phys. Lett. B* **777**, 91 (2018), [arXiv:1708.04445 \[hep-ex\]](#).
 - [32] M. Aaboud *et al.* (ATLAS), *Phys. Rev. D* **98**, 052008 (2018), [arXiv:1808.02380 \[hep-ex\]](#).
 - [33] M. Aaboud *et al.* (ATLAS), *Eur. Phys. J. C* **78**, 24 (2018), [arXiv:1710.01123 \[hep-ex\]](#).
 - [34] G. Aad *et al.* (ATLAS), *Phys. Rev. Lett.* **125**, 051801 (2020), [arXiv:2002.12223 \[hep-ex\]](#).
 - [35] M. Aaboud *et al.* (ATLAS), *JHEP* **01**, 055 (2018), [arXiv:1709.07242 \[hep-ex\]](#).
 - [36] T. Huang, J. M. No, L. Pernié, M. Ramsey-Musolf, A. Safonov, M. Spannowsky, and P. Winslow, *Phys. Rev. D* **96**, 035007 (2017), [arXiv:1701.04442 \[hep-ph\]](#).
 - [37] J. R. Espinosa, T. Konstandin, and F. Riva, *Nucl. Phys. B* **854**, 592 (2012), [arXiv:1107.5441 \[hep-ph\]](#).
 - [38] H. H. Patel and M. J. Ramsey-Musolf, *JHEP* **07**, 029 (2011), [arXiv:1101.4665 \[hep-ph\]](#).
 - [39] M. Laine, *Phys. Rev. D* **51**, 4525 (1995), [arXiv:hep-ph/9411252](#).
 - [40] A. Ekstedt and J. Löfgren, *JHEP* **01**, 226 (2019), [arXiv:1810.01416 \[hep-ph\]](#).
 - [41] M. Garny and T. Konstandin, *JHEP* **07**, 189 (2012), [arXiv:1205.3392 \[hep-ph\]](#).
 - [42] M. Carena, Z. Liu, and Y. Wang, *JHEP* **08**, 107 (2020), [arXiv:1911.10206 \[hep-ph\]](#).
 - [43] J. Kozaczuk, M. J. Ramsey-Musolf, and J. Shelton, *Phys. Rev. D* **101**, 115035 (2020), [arXiv:1911.10210 \[hep-ph\]](#).
 - [44] A. Alves, T. Ghosh, H.-K. Guo, K. Sinha, and D. Vagie, *JHEP* **04**, 052 (2019), [arXiv:1812.09333 \[hep-ph\]](#).
 - [45] G. Kurup and M. Perelstein, *Phys. Rev. D* **96**, 015036 (2017), [arXiv:1704.03381 \[hep-ph\]](#).
 - [46] C.-Y. Chen, J. Kozaczuk, and I. M. Lewis, *JHEP* **08**, 096 (2017), [arXiv:1704.05844 \[hep-ph\]](#).
 - [47] C.-Y. Chen, S. Dawson, and I. M. Lewis, *Phys. Rev. D* **91**, 035015 (2015), [arXiv:1410.5488 \[hep-ph\]](#).
 - [48] A. Katz and M. Perelstein, *JHEP* **07**, 108 (2014), [arXiv:1401.1827 \[hep-ph\]](#).
 - [49] P. H. Damgaard, A. Haarr, D. O'Connell, and A. Tranberg, *JHEP* **02**, 107 (2016), [arXiv:1512.01963 \[hep-ph\]](#).
 - [50] P. Huang, A. Joglekar, B. Li, and C. E. M. Wagner, *Phys. Rev. D* **93**, 055049 (2016), [arXiv:1512.00068 \[hep-ph\]](#).

- [51] D. Curtin, P. Meade, and C.-T. Yu, *JHEP* **11**, 127 (2014), [arXiv:1409.0005 \[hep-ph\]](#).
- [52] J. M. No and M. Ramsey-Musolf, *Phys. Rev. D* **89**, 095031 (2014), [arXiv:1310.6035 \[hep-ph\]](#).
- [53] W. Huang, J. Shu, and Y. Zhang, *JHEP* **03**, 164 (2013), [arXiv:1210.0906 \[hep-ph\]](#).
- [54] P. H. Damgaard, D. O’Connell, T. C. Petersen, and A. Tranberg, *Phys. Rev. Lett.* **111**, 221804 (2013), [arXiv:1305.4362 \[hep-ph\]](#).
- [55] A. Ashoorioon and T. Konstandin, *JHEP* **07**, 086 (2009), [arXiv:0904.0353 \[hep-ph\]](#).
- [56] A. Noble and M. Perelstein, *Phys. Rev. D* **78**, 063518 (2008), [arXiv:0711.3018 \[hep-ph\]](#).
- [57] J. R. Espinosa and M. Quiros, *Phys. Rev. D* **76**, 076004 (2007), [arXiv:hep-ph/0701145](#).
- [58] J. M. Cline and K. Kainulainen, *JCAP* **01**, 012 (2013), [arXiv:1210.4196 \[hep-ph\]](#).
- [59] S. Profumo, M. J. Ramsey-Musolf, C. L. Wainwright, and P. Winslow, *Phys. Rev. D* **91**, 035018 (2015), [arXiv:1407.5342 \[hep-ph\]](#).
- [60] C. L. Wainwright, *Comput. Phys. Commun.* **183**, 2006 (2012), [arXiv:1109.4189 \[hep-ph\]](#).
- [61] H.-L. Li, M. Ramsey-Musolf, and S. Willocq, *Phys. Rev. D* **100**, 075035 (2019), [arXiv:1906.05289 \[hep-ph\]](#).
- [62] M. Aaboud *et al.* (ATLAS), *Eur. Phys. J. C* **78**, 110 (2018), [Erratum: *Eur.Phys.J.C* 78, 898 (2018)], [arXiv:1701.07240 \[hep-ex\]](#).
- [63] M. Cepeda *et al.*, *CERN Yellow Rep. Monogr.* **7**, 221 (2019), [arXiv:1902.00134 \[hep-ph\]](#).
- [64] J. Alwall, M. Herquet, F. Maltoni, O. Mattelaer, and T. Stelzer, *JHEP* **06**, 128 (2011), [arXiv:1106.0522 \[hep-ph\]](#).
- [65] T. Sjostrand, S. Mrenna, and P. Z. Skands, *Comput. Phys. Commun.* **178**, 852 (2008), [arXiv:0710.3820 \[hep-ph\]](#).
- [66] J. de Favereau, C. Delaere, P. Demin, A. Giammanco, V. Lemaître, A. Mertens, and M. Selvaggi (DELPHES 3), *JHEP* **02**, 057 (2014), [arXiv:1307.6346 \[hep-ex\]](#).
- [67] M. Cacciari, G. P. Salam, and G. Soyez, *JHEP* **04**, 063 (2008), [arXiv:0802.1189 \[hep-ph\]](#).
- [68] S. Chatrchyan *et al.* (CMS), *JINST* **8**, P04013 (2013), [arXiv:1211.4462 \[hep-ex\]](#).
- [69] M. E. Peskin and T. Takeuchi, *Phys. Rev. Lett.* **65**, 964 (1990).
- [70] M. E. Peskin and T. Takeuchi, *Phys. Rev. D* **46**, 381 (1992).
- [71] M. Baak, J. Cúth, J. Haller, A. Hoecker, R. Kogler, K. Mönig, M. Schott, and J. Stelzer (Gfitter Group), *Eur. Phys. J. C* **74**, 3046 (2014), [arXiv:1407.3792 \[hep-ph\]](#).
- [72] T. Aaltonen *et al.* (CDF), *Science* **376**, 170 (2022).
- [73] J. de Blas, M. Pierini, L. Reina, and L. Silvestrini, (2022), [arXiv:2204.04204 \[hep-ph\]](#).